Multiple dimeric structures and strand-swap dimerization of E-cadherin in solution visualized by high-speed atomic force microscopy

Shigetaka Nishiguchi[a,1] (iD), Tadaomi Furuta[b] (iD), and Takayuki Uchihashi[a,c,d,1] (iD)

Classical cadherins play key roles in cell–cell adhesion. The adhesion process is thought to comprise mainly two steps: X-dimer and strand-swap (SS-) dimer formation of the extracellular domains (ectodomains) of cadherins. The dimerization mechanism of this two-step process has been investigated for type I cadherins, including E-cadherin, of classical cadherins, whereas other binding states also have been proposed, raising the possibility of additional binding processes required for the cadherin dimerization. However, technical limitations in observing single-molecule structures and their dynamics have precluded the investigation of the dynamic binding process of cadherin. Here, we used high-speed atomic force microscopy (HS-AFM) to observe full-length ectodomains of E-cadherin in solution and identified multiple dimeric structures that had not been reported previously. HS-AFM revealed that almost half of the cadherin dimers showed S- (or reverse S-) shaped conformations, which had more dynamic properties than the SS- and X-like dimers. The combined HS-AFM, mutational, and molecular modeling analyses showed that the S-shaped dimer was formed by membrane-distal ectodomains, while the binding interface was different from that of SS- and X-dimers. Furthermore, the formation of the SS-dimer from the S-shaped and X-like dimers was directly visualized, suggesting the processes of SS-dimer formation from S-shaped and X-dimers during cadherin dimerization.

cadherin dimerization | single-molecule dynamics | HS-AFM

Classical cadherins are responsible for binding to dynamic membrane surfaces in opposing cells via extracellular cadherin (EC) domains (ectodomains), which are essential for the calcium-dependent binding of cadherins (1–3). The mutual binding of EC domains is necessary for embryonic development and tissue formation, and defects in binding cause severe diseases (4–6). The structures and binding mechanisms of classical type I cadherins, including E-cadherin, have been well studied (7–9). Type I cadherins possess five tandem EC domains (EC1 to EC5), a transmembrane region, and a catenin-binding cytoplasmic domain that indirectly interacts with the cytoskeleton. The "*trans*-binding" of type I cadherins between opposing cells is considered to be formed by a two-step binding process (10–14). First, regions near the calcium-binding linker of membrane-distal EC1–EC2 bind to each other via a salt bridge between Lys14 and Asp138, forming an X-dimer (10, 13, 15, 16). Second, each EC1 swaps a Trp2 of the N-terminal β-strand with the hydrophobic acceptor pocket of its partner EC1, forming a strand-swap dimer (SS-dimer) (17–20). The formation of an SS-dimer is an endpoint in the dimerization process, which requires X-dimer formation to bring each EC1 close to its partner EC1, thereby decreasing the kinetic barrier of strand-swap dimerization (11, 13, 21). The X-dimer also functions as a mechano-sensor; when the dimer is pulled apart, the interaction becomes stronger via a catch-bond mechanism (22–24). In addition, the type I cadherins form "*cis*-binding" in which Val81 in EC1 and Leu175 in EC2 of the adjacent molecules on the same membrane surface interact hydrophobically; this binding is essential for the formation of cadherin clusters (17, 25–27).

Although the *trans*-binding of the X- and SS-dimers and *cis*-binding of type I cadherins have been demonstrated by structural, functional, and simulation studies, interactions other than those of the X- and SS-dimers and *cis*-binding have also been proposed (20, 28–31). Previous studies using X-ray crystallography have suggested potential interactions between EC1 and EC1 of N-cadherin, and EC1 and EC2 of P-cadherin, formed by different binding interfaces from X- and SS-dimers and *cis*-binding (20, 29). Furthermore, force spectroscopies and bead aggregation assays have revealed the contributions of EC1 and EC2 as well as other EC domains in cadherin binding (28, 30, 31). These studies suggest that type I cadherins form multiple binding structures during

Significance

E-cadherin is a major cell–cell adhesion molecule that connects opposing cells via extracellular domains (ectodomains) and regulates tissue morphology and dynamics. Mutual binding of the ectodomains has been considered to be formed by a strand-swap (SS-) dimer via an X-dimer; however, the dimerization processes have not been directly visualized, and other potential dynamic interactions have been proposed. In this study, high-speed atomic force microscopy (HS-AFM), mutational analyses, and structural modeling revealed the dimeric structures that are mainly classified into SS- (W-shaped), X-like (cross-shaped), and S-shaped (or reverse S-shaped) dimers. The structural transition from the S-shaped and X-like dimers to the SS-dimer formation, visualized by HS-AFM, suggests the contribution of dynamic interactions to the SS-dimer formation of E-cadherin in solution.

the binding processes. However, the lack of techniques to observe the structures and dynamics at the single-molecule level in solution has made it difficult to study potential binding structures and dynamic binding processes of cadherins. High-speed atomic force microscopy (HS-AFM) is a powerful tool to investigate the structures and dynamics of single molecules in solution at a nanometer scale with subsecond time resolution (32, 33). In this study, we investigated the binding structures of the full-length ectodomains (EC1 to EC5) of E-cadherin in solution and explored its dynamic binding processes by HS-AFM, mutational analyses, and structural modeling.

Results

HS-AFM Visualization of the Structures and Dynamics of E-Cadherin Ectodomains in Solution. First, we purified the full-length ectodomains (EC1 to EC5) of mouse E-cadherin from mammalian cells (HEK293T cells) and confirmed the calcium-dependent binding activity by a bead aggregation assay (*SI Appendix,* Fig. S1). We then observed the ectodomains adsorbed on the mica surface in the same buffer solution (20 mM Hepes, 4 mM CaCl$_2$, and pH 6.8) as the one used for the bead aggregation assay. The HS-AFM images showed a slightly curved rod-like structure and dynamic twisting motion of the ectodomains (Fig. 1*A*, *SI Appendix,* Fig. S2, and Movie S1). To visualize individual cadherin molecules clearly by HS-AFM, the sample solution was diluted to nanomolar concentrations before adsorption onto the mica substrate. At such low concentrations, more than 90% of the molecules were observed as monomers because of their low binding affinity (K_d: 80 to 98.6 μM) (1, 34, 35). The remaining molecules (<10%) were dimeric. A total of 71 dimers were observed by HS-AFM. The structural dynamics of each dimer were first evaluated by an SD (σ_φ) of angles (φ) between

the major axes of protomers in sequential images using up to 20 frames of HS-AFM images from the beginning of the recording. The evaluation revealed that the observed dimers were divided into "dynamic" and "static" dimers by a threshold of σ_φ of 15°, where the populations of dynamic and static dimers were 35% and 65%, respectively (*SI Appendix,* Fig. S3*A and B*). The dynamic dimers showed flexible angle changes with time, while the static dimers were stable without large angle changes (Fig. 1*B–D* and Movies S2 and S3). The distribution of the protomer angles (φ) of all the dynamic dimers ($\sigma_\varphi \geq 15°$) using the sequential images evaluated above showed two main components: the major component (majority), with large angles of $\varphi \geq 86°$ and minor component with small angles of $\varphi < 86°$ (*SI Appendix,* Fig. S3*C*). Moreover, the majority analyzed here (corresponding to 31% among 35% of dynamic dimers) had a distinctive S-shaped (or reverse S-shaped) appearance (Fig. 1*B* and *SI Appendix,* Fig. S3*C*). These distinctive dimers are hereafter referred to as "S-shaped" dimer.

On the other hand, the static dimers ($\sigma_\varphi < 15°$) had more diverse conformations, while the majority (34% among 65% of static dimers) of these dimers exhibited "W-shaped" conformations with a single height peak of the binding interface, which retained the conformations while moving on the substrate during long time durations (Fig. 1*B–D*, *SI Appendix,* Fig. S3*A*, and Movie S3). Furthermore, it was found that the S-shaped dimer (observed in dynamic dimers with large angles of $\varphi \geq 86°$ and a distinctive S-shaped appearance) was included also in the static dimers (corresponding to 15% among 65% of static dimers). This was mainly because these dimers were dissociated during short time durations or fixed on the substrate without conformational changes, suggesting a limitation of characterization of different dimeric conformations based on the dynamics. Therefore, the observed dimers were classified into W-shaped
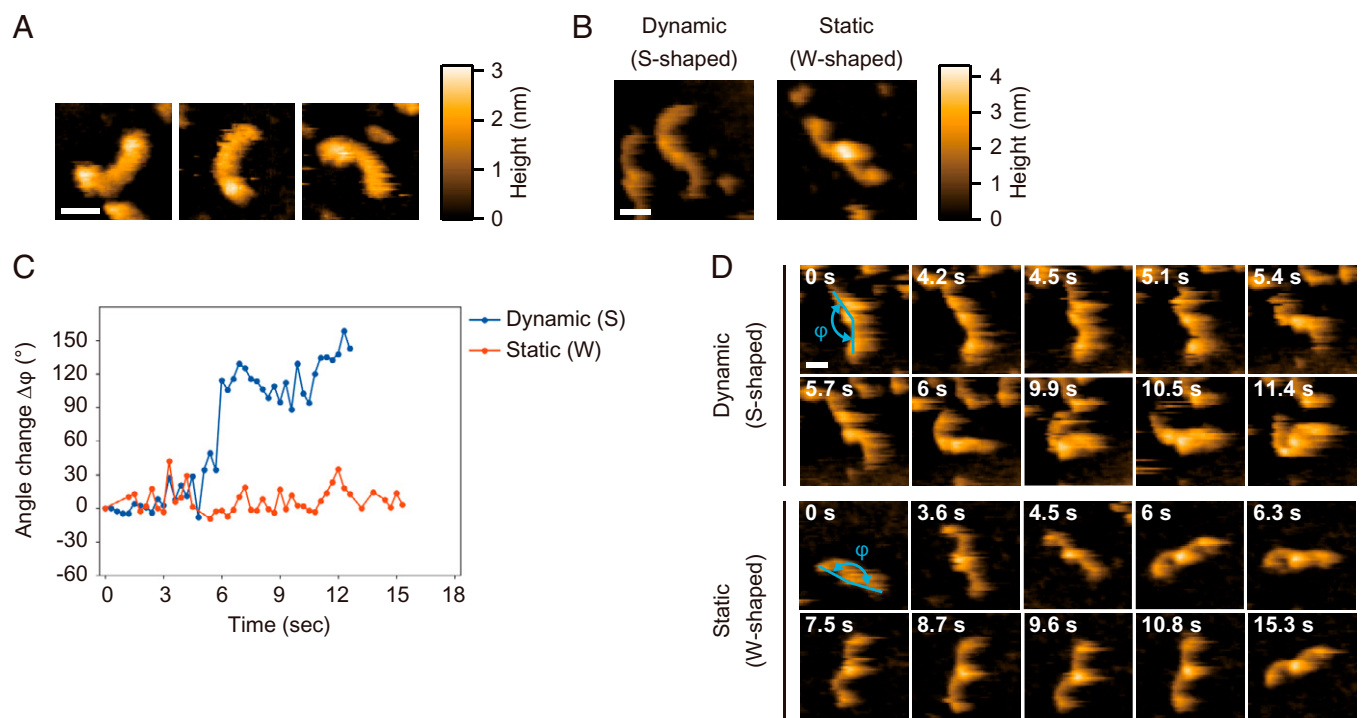

Fig. 1. Dynamic and static dimers of full-length ectodomains of E-cadherin observed by HS-AFM. (*A*) Representative images of monomers of the ectodomains. (*B*) Representative images of dynamic (S-shaped) and static (W-shaped) dimers. (*C*) Line graph showing angle change Δφ of the dynamic and static dimers. "φ" represents the angles between the major axes of the protomers (blue lines in *D*). The data for the dynamic and static dimers correspond with the S-shaped and W-shaped dimers, respectively, in *D*. (*D*) Representative images of the structural dynamics of S- and W-shaped dimers. (Scale bars, 10 nm.) Images shown are representative of six experiments. More examples are included in *SI Appendix,* Figs. S2–S4. See also Movies S2 and S3.

(34%), S-shaped (46%), and others (20%). Thus, the HS-AFM analysis revealed that the ectodomains coexist as multiple dimeric structures with several different features.

Identification of SS- and X-Like Dimers by Mutational Analyses and Structural Modeling. To examine the relationships between the dimers observed by HS-AFM and known dimer structures—that is, SS- and X-dimers—we observed the dimers of the SS-dimer–incompetent W2A mutant that differed from the WT only in the second amino acid (Trp2) of the mature ectodomains (10, 13). The HS-AFM images of the W2A mutant (total 60 dimers) showed a complete disappearance of the W-shaped dimers, while the percentage of the S-shaped dimers (45%) was similar to that in the WT (46%) (*SI Appendix,* Figs. S4 and S5). The observations of the W2A also revealed a notable increase in dimers with a specific shape in which an axis connecting two height peaks near the binding interfaces of dimers was nearly perpendicular (ψ~90°) to an axis connecting two opposite sides of protomers from the binding interface. This shape is hereafter referred to as "cross-shaped" (*SI Appendix,* Figs. S3D, S4, and S5). The percentage of the cross-shaped dimers in the W2A mutant was 20% while that in the WT was 3%. These dimers were reclassified as cross-shaped to distinguish them from the others mentioned

above (Fig. 2A). The cross-shaped dimers were also static while retaining the conformations during long time durations, similar to the W-shaped dimers (Movie S4). The complete disappearance of the W-shaped dimers in the SS-dimer–incompetent W2A indicated that the W-shaped dimers observed in the WT likely corresponded to the SS-dimers (Fig. 2A). It was also confirmed that the ratio of the W-shaped dimers decreased in the W2F mutant, with a smaller Phe2 side chain providing weaker constraints in the acceptor pocket of the SS-dimers, as previously reported (Fig. 2A and *SI Appendix,* Fig. S6) (12, 14, 36) (total 47 dimers) (12, 14, 36).

To compare the observed dimer structures with the crystal structure of the SS-dimer, pseudo-AFM images were generated using the crystal structures of the SS-dimer of E-cadherin (10, 25). We first created the SS-dimer model consisting of full-length E-cadherin ectodomains (EC1 to EC5) (Fig. 2B and *SI Appendix,* Fig. S7A). To find the most likely orientation of the molecule corresponding to the observed AFM images, we rotated the model structure from 0° (a set position) to 180° around the x axis and generated pseudo-AFM images (*SI Appendix,* Fig. S7A). Among these pseudo-AFM images, those similar to the actual HS-AFM images of the SS-dimers in WT showed single height peaks at the bonding interface (0 to 90°) (Fig. 2B and C and *SI Appendix,* Fig. S7A). The average value
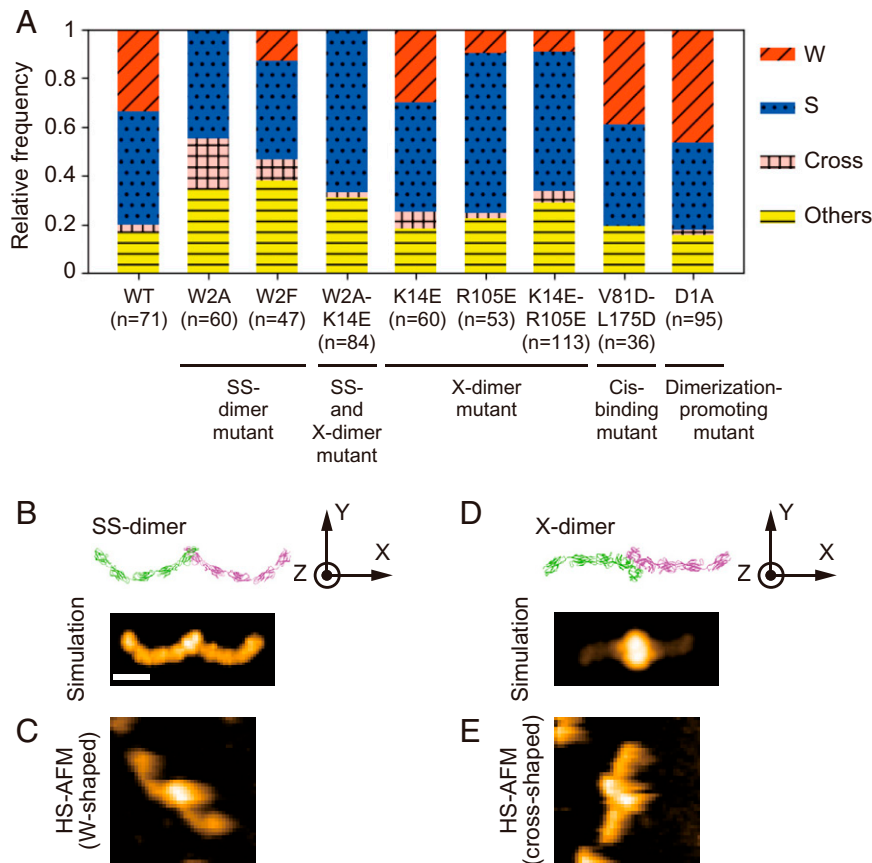
Fig. 2. Mutational analyses and structural modeling of E-cadherin. (A) Cumulative bar chart showing the relative frequency of cases with W-, S-, cross-shaped, and other dimers in WT and mutant proteins. The mutant proteins were analyzed in two or more experiments. See *SI Appendix,* Figs. S4–S6, S8–S12, and S15. (B) Pseudo-AFM image of the SS-dimer of the full-length ectodomains of E-cadherin (90° in *SI Appendix,* Fig. S7A). The upper image is the crystal structure generated using 3Q2V and 2QVF from the protein data bank. The structures consisting of full-length ectodomains (EC1–EC5) of E-cadherin were modeled by fitting the EC1–EC2 parts of the full-length ectodomains (PDB ID code: 3Q2V chain A) to both sides of the SS-dimer formed by EC1–EC2 (PDB ID code: 2QVF). The lower image is the pseudo-AFM image generated from the upper image. (C) HS-AFM image of the W-shaped dimer of WT. (D) Pseudo-AFM image of X-dimer of the full-length ectodomains of E-cadherin (0° in *SI Appendix,* Fig. S7D). The structures consisting of full-length ectodomains (EC1 to EC5) of E-cadherin were modeled by fitting the EC1–EC2 parts of the full-length ectodomains (PDB ID code: 3Q2V chain A) to both sides of the X-dimer formed by EC1–EC2 (PDB ID code 3LNH). The lower image is the pseudo-AFM image generated from the upper image. (E) HS-AFM image of the cross-shaped dimer of the W2A mutant. (Scale bar, 10 nm.) All images are displayed at the same scale except for the crystal structures. See *SI Appendix,* Fig. S7.

of maximum height of the single peak of the HS-AFM images (3.8 ± 0.1 nm; $n = 24$) was close to that of the pseudo-AFM images at 90° (4.1 nm) (*SI Appendix*, Fig. S7*B* and *C*). Overall, the results for the W2A and W2F mutants and structural modeling show that the W-shaped dimers observed by HS-AFM correspond to the SS-dimers.

For the W2A mutant, the increase (17%) in the cross-shaped dimers suggests a relationship between the cross-shaped and the X-dimers because the X-dimer conformation is trapped by the inhibition of SS-dimer formation due to the W2A mutation (Fig. 2*A*) (10, 24). To confirm whether mutations of other key residues of the X-dimer affect the appearance of the cross-shaped dimer, we also observed the SS- and X-dimer–incompetent W2A–K14E mutant (10, 24). Of the 84 dimers observed for the W2AK–14E mutant, the W-shaped dimers completely disappeared, as in case of the W2A mutant, while the proportion of cross-shaped dimers (2%) decreased by 18% compared to that of the W2A mutant (20%) (Fig. 2*A* and *SI Appendix*, Fig. S8). The results for the W2A and W2A–K14E mutants indicate a close relationship between the cross-shaped and X-dimers.

Next, to find the most likely orientations of the observed cross-shaped dimers, in the same way as described above, pseudo-AFM images of the X-dimers were generated and compared to those of the cross-shaped dimers observed in the W2A mutant (Fig. 2*D* and *E* and *SI Appendix*, Fig. S7*D*). The actual HS-AFM images most closely resemble the simulation image at the set position (0°) (Fig. 2*D* and *E* and *SI Appendix*, Fig. S7*D*). However, the heights of the HS-AFM images (2.8 ± 0.1 nm; $n = 12$) were much smaller than those of the pseudo-AFM image (14.3 nm) (*SI Appendix*, Fig. S7*F* and *H*). Moreover, the distances between the two peaks representing the heights of the membrane-distal tip portions of the ectodomains of the HS-AFM images (5.8 ± 0.2 nm; $n = 12$) were larger than those of the pseudo-AFM images (3.4 nm) (*SI Appendix*, Fig. S7*F* and *H*). These discrepancies may have been because the proximal sides of the ectodomains on the membranes adsorbed flatly on the mica substrate without firm contact with the distal tips of the membrane, while maintaining the dimeric form of the X-dimer or X-dimer–like conformations. The flexibility observed in the monomeric ectodomains (*SI Appendix*, Fig. S2*B* and *C*) supports that the deformation of the ectodomains on the mica substrate is possible without disrupting the dimeric form.

To explore the similarity of the cross-shaped dimer to the X-dimer, we further modified the model structure by adjusting the EC2–EC3 linker of the model structure to orient the EC3–EC5 region more flatly on the substrate (*SI Appendix*, Fig. S7*E*). A pseudo-AFM image of the modified model showed a quite similar morphology to the HS-AFM image. The maximum height of the binding interface (9.2 nm) became closer to that of the cross-shaped dimers than of the previous model (14.3 nm), although the heights and distances of two height peaks were still not matched sufficiently to the cross-shaped dimers (*SI Appendix*, Fig. S7*G* and *H*). Overall, the results for the W2A and W2A–K14E mutants and structural modeling indicate that the cross-shaped dimers observed by HS-AFM were related to the X-dimers, although a small population of the cross-shaped dimers was still observed in W2A–K14E. In addition, the variants K14E, R105E, and K14E–R105E, which could be single or double salt bridge-breaking mutants (Lys14–Asp138 and Arg105–Glu199) based on the crystal structure of the X-dimer (10), were also found to have small populations of the cross-shaped dimer (Fig. 2*A* and *SI Appendix*, Figs. S9–S11) (total 60, 53, and 113 dimers, respectively).

The bead aggregation assay revealed that small bead aggregations were formed in W2A whereas they were abolished in W2A–K14E and other salt bridge-breaking mutants (*SI Appendix*, Fig. S1*B*). The results of the HS-AFM observation and bead aggregation assay suggest that the binding strength of the cross-shaped dimers in the salt bridge-breaking mutants (and also S-shaped dimers) observed by the HS-AFM would be weak to hold bead aggregation. Previous studies have reported that the salt bridge formed between Lys14 and Asp138 is important for the strong binding of the X-dimer (24), while the salt bridge would disappear for SS-dimer formation (12). Overall, these results suggest that the HS-AFM visualized the X-dimer or X-dimer–like conformations, as the cross-shaped dimers and could not distinguish these different dimeric conformations, due to the resolution limitation (>2 nm). Therefore, we described the cross-shaped dimer observed by the HS-AFM as the "X-like" dimer in this study.

S-Shaped Dimers Formed by the Membrane-Distal Ectodomains and Different Binding Interfaces from *cis*-Binding. The HS-AFM images showed that approximately half of the population of the dimers were S-shaped in the WT, SS-, and X-dimer mutants (Fig. 2*A*). From the pseudo-AFM images based on the crystal structure described above, it seems unlikely that the SS- and X-dimers could be imaged as S- or reverse-S-shaped conformations (*SI Appendix*, Fig. S7*A* and *D*), indicating that the S-shaped dimer was not an SS- or X-dimer. Since the *cis*-binding of the ectodomains of type I classical cadherins on the same membrane has been previously reported (17, 25, 26), we observed the *cis*-binding–incompetent V81D–L175D mutant to confirm the possibility that the S-shaped dimers could be formed by the *cis*-binding interface. The results showed that the population ratio of the dimer shapes was similar to that of the WT (Fig. 2*A* and *SI Appendix*, Fig. S12) (total 36 dimers), indicating that the inhibition of the *cis*-binding interfaces did not affect the appearance of the S-shaped dimers. To locate the binding side of the protomers of the S-shaped dimers, we observed WT tagged with green fluorescent protein (GFP) on the membrane-proximal side (WT-GFP). This was because the diameter of GFP was twice as large (~4 nm) as the short axis of each EC domain (~2 nm), which allowed us to identify the distal and proximal membrane sides of the ectodomain (25, 37). The HS-AFM images of WT-GFP showed a large globular
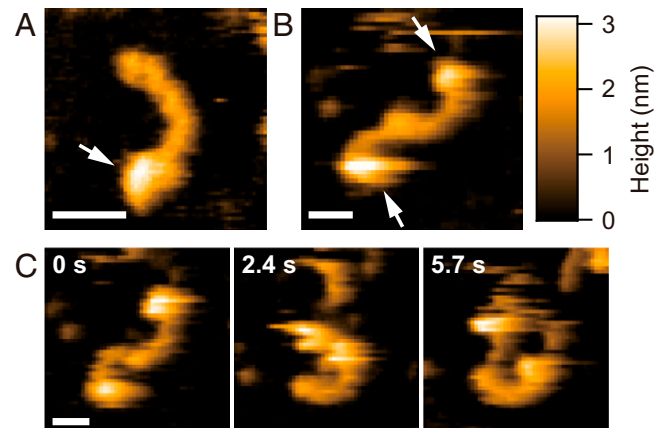
Fig. 3. HS-AFM images of E-cadherin tagged with GFP in the membrane-proximal side. (*A* and *B*) A representative image of monomer (*A*) and dimer (*B*) of the ectodomains. White arrows point to GFP portions. (*C*) Representative images of conformational change of S-shaped dimers of the ectodomains. (Scale bars, 10 nm.) Images shown are representative of three experiments. More examples are included in *SI Appendix*, Fig. S13. See also Movie S5.

portion on one side of the ectodomains (Fig. 3*A* and *SI Appendix*, Fig. S13*A*). In the S-shaped dimers formed by WT-GFP, the GFPs were located on the opposite side of the binding interface. Dynamic conformational changes were observed in the same manner as in the WT (Fig. 3*B* and *C*, *SI Appendix*, Fig. S13*B*, and Movie S5).

Structural Transition of SS-Dimers Visualized by HS-AFM. The HS-AFM images of the WT revealed a transition from S-shaped to SS- (W-shaped) dimers, S-shaped to X-like (cross-shaped) dimers, and SS- to X-like dimers (*SI Appendix*, Fig. S14 and Movies S6–S8). Furthermore, the X-like dimers of the W2A mutant changed the interface to the membrane-proximal side (*SI Appendix*, Fig. S14 and Movie S9). The transition suggests that different dimeric conformations are involved in the dimerization processes of cadherins; however, the low probability of structural transitions prevented us from investigating the relationships between the different dimeric structures in detail. Therefore, we observed the D1A mutant, which is considered to be a dimerization-promoting mutant, by immunoprecipitation experiments and cell measurements (Figs. 2*A* and 4 and *SI Appendix*, Fig. S15) (38–40). The different dimeric conformations of the sequential HS-AFM images were classified in each frame based on the same classification procedures used for the WT and mutants. The HS-AFM images showed a clear transition of the D1A dimers among the SS-, X-like, and S-shaped dimer conformations (Fig. 4 and Movie S10). The analyses revealed that SS-dimer formation and dissociation from S-shaped or X-like dimer conformations were completed within 0.9 s for three frames (0.3 s per frame). This supports previous studies that used NMR spectroscopy (NMR), which showed that the dimerization and dissociation processes of SS-dimers took ~1 s (11). Furthermore, both the X-like and S-shaped dimers were mainly transiently observed in each single frame of 0.3 s during SS-dimer formations (Fig. 4 and *SI Appendix*, Fig. S15*B*), while the X-like dimers also retained the conformations in long time durations while moving on the substrate in other cases (Movie S4). This suggests that the X-like dimers have both static and dynamic states.

S-Shaped Dimers Formed in Low Calcium Conditions. We observed that the dimeric and monomeric (rod-like) structures observed in the presence of Ca^{2+} (Fig. 1*A* and *B*) completely disappeared in the presence of EGTA (Ca^{2+}-chelating). The disordered morphology consisted of small globules connected by string-like structures (Fig. 5*A*). While observing the conformations of the WT monomers in 1 mM Ca^{2+} buffer, we added EGTA to the buffer until a final concentration of 3 mM was reached. The HS-AFM images showed that the rod-like structures transitioned into small globules connected by the string-like structures, indicating that some of the ectodomains were unfolded (Fig. 5*B* and Movie S11). To further investigate the effect of Ca^{2+} on the dimeric structure, we observed the WT dimers at a low calcium concentration of 10 μM, which is below the average affinity of the calcium linkers for Ca^{2+} (K_d: ~30 μM) (1). In the low Ca^{2+} buffer, the SS- (W-shaped) dimers were completely abolished, whereas one X-like (cross-shaped) dimer and 50 S-shaped dimers were observed (Fig. 5*C* and *SI Appendix*, Fig. S16). This indicates that the binding of S-shaped dimers is not affected by fluctuations in the calcium binding sites of ectodomains owing to low Ca^{2+} concentrations.

Discussion

In this study, HS-AFM, mutational analyses, and structural modeling revealed the coexistence of multiple dimeric structures that were mainly classified into SS- (W-shaped), X-like (cross-shaped), and S-shaped (or reverse S-shaped) dimers, which have not been previously reported. The structural transition from the S-shaped, and X-like dimer conformations to the SS-dimers, visualized by HS-AFM, suggests that dynamic interactions of the S-shaped dimer contribute to SS-dimer formations in the binding processes of cadherin dimerization. S-shaped conformations of desmosomal cadherins have been previously studied by electron tomography (41, 42), supporting the existence of the S-shaped dimers of E-cadherin in the classical cadherins observed in this study. With conventional AFM, however, only the W-shaped dimer has been reported in the E-cadherin–Fc fusion protein, and the relationship to the dimeric structures seen in the crystal and
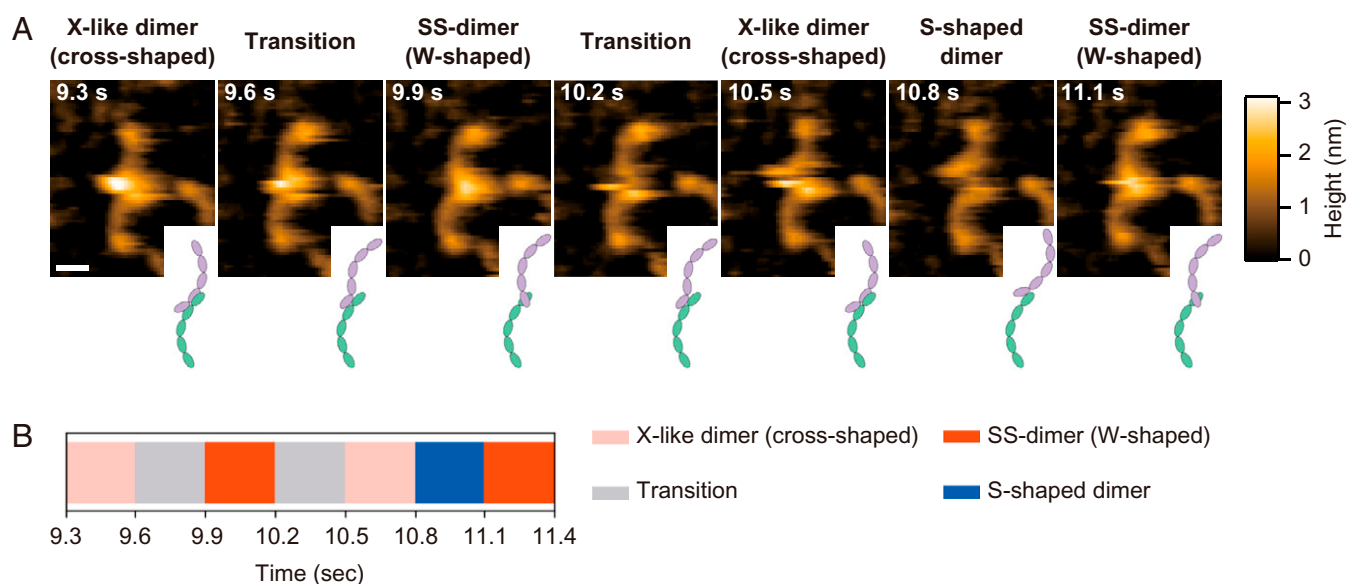
Fig. 4. Structural transitions of SS- (W-shaped) dimers visualized by HS-AFM. (*A*) Representative images of structural transitions among SS- (W-shaped), S-shaped dimers, and X-like (cross-shaped) dimers in the D1A mutant. Dimers in which it was difficult to define the shapes in intermediate phases are referred to as "Transition." (Scale bar, 10 nm.) (*B*) Horizontal bar chart showing dimer shapes classified in each frame in *A*. The classification results of whole images are shown in *SI Appendix*, Fig. S15*B*. See also Movie S10.
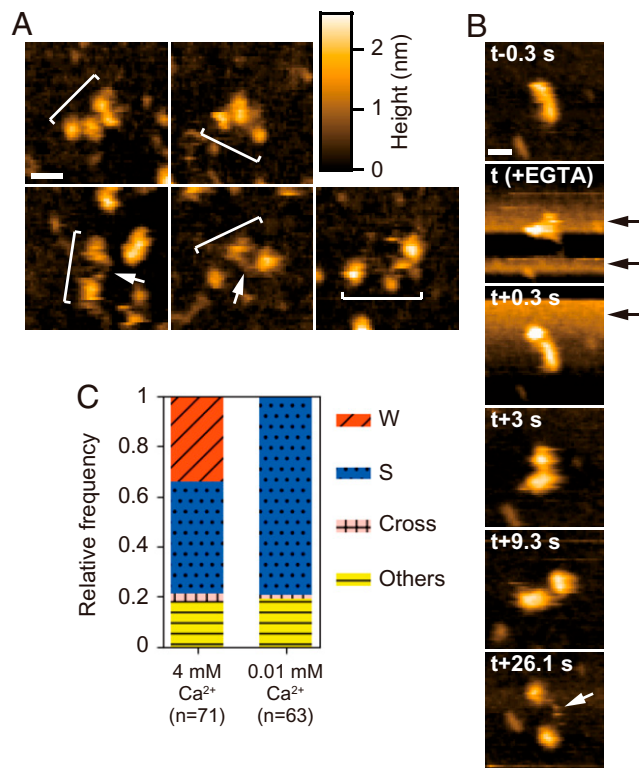
Fig. 5. HS-AFM observation of E-cadherin in EGTA and low calcium conditions. (*A*) Disordered morphologies of the ectodomains in EGTA. White brackets indicate single-monomers. White arrows point to the string-like structures connecting the small globules of single-monomers. Images shown are representative of three experiments. (*B*) Sequential images of monomers of the ectodomains after EGTA addition to the calcium buffer. "t" indicates the time of the EGTA injection. Black arrows point to scanning noises due to EGTA addition. See Movie S11. (*C*) Cumulative bar chart showing relative frequency of cases with W-, S-, cross-shaped, and other dimers in the WT at 4 and 0.01 mM (10 μM) Ca²⁺. HS-AFM images of the WT in 10 μM Ca²⁺ are in included *SI Appendix*, Fig. S16. (Scale bars, 10 nm.)

dynamics of the W-shaped dimer have not been fully investigated (43). In the previous study, the S-shaped and X-like dimers observed by our HS-AFM may have been disrupted on mica substrates using conventional AFM due to conformational constraints on the mica substrates by Fc conjugation, which artificially connects two cadherins at the membrane-proximal sides of the ectodomains. A strong adsorption of proteins on the mica substrates using the hydrophobic coating of the substrates for low-speed imaging (∼3 min per frame) (43) also could have disrupted the S-shaped and X-like dimers. Multiple dimeric structures and the structural dynamics of cadherin while maintaining dimeric bonds demonstrate that our high-speed imaging (0.2 to 0.4 s per frame) was minimally invasive for cadherin dimers.

Structures of SS- and X-Like Dimers in Solution. In the W2A and W2A–K14E mutants, in which mutations were introduced into the key residues of the swapping strand (Trp2) of the SS-dimer and a salt bridge (Lys14) of the X-dimer, the W-shaped dimers were fully lost, indicating that the W-shaped dimer was the SS-dimer (Fig. 2*A*). The increase and decrease of the cross-shaped dimers in the W2A and W2A–K14E mutants showed that the cross-shaped dimer was related to the X-dimer, although small populations of the cross-shaped dimers were also found in the salt bridge-breaking mutants (W2A–K14E, K14E, R105E, and K14E–R105E) (Fig. 2*A*). The bead aggregation assay revealed that small bead aggregations were formed in W2A, whereas the bead aggregation was abolished in W2A–K14E and

other salt bridge-breaking mutants, suggesting that the cross-shaped dimers in the salt bridge-breaking mutants and S-shaped dimers were not sufficient to hold bead aggregation (*SI Appendix,* Fig. S1*B*). The results of the small populations of the cross-shaped dimers observed in the salt bridge-breaking mutants (including K14E and R105E mutation) may have been counterintuitive, because the X-dimer was stabilized by the salt bridges, as previously reported (10, 15, 16).

Previous studies have shown that, in the crystal structures of the X-dimer, there are salt bridges between Lys14 and Asp138, and Arg105 and Glu199, as well as hydrogen bonds and non-polar interactions (10, 15, 16). One salt bridge has been noted to form between Lys14 and Asp138 but the other is broken in the X-dimer crystal structure (W2A mutant; PDB ID code: 3LNH). Furthermore, previous studies using force spectroscopy and molecular dynamics (MD) simulations have reported that the salt bridge between Lys14–Asp138 in the X-dimer conformation disappears to form the SS-dimer conformation, while the binding strength of the X-dimer depends on the salt bridge (12, 24). Therefore, although the functional significance of Lys14 for the X-dimer is supported by comprehensive studies (10–12, 24, 38), the small population of the cross-shaped dimer in the salt bridge-breaking mutants suggests that the X-dimer–like conformation can be formed by other native residues without a single pair of salt bridges. We assumed that previous studies could not detect the X-dimer–like conformation due to weak binding or small populations of them under the detection limitation of other experiments. Our results showed that the HS-AFM visualized the X-dimer or X-dimer–like conformations like the cross-shaped dimer. However, because the HS-AFM could not distinguish the different dimeric conformations due to the resolution limitation (>2 nm), we defined the cross-shaped dimer as "X-like" in this study. Moreover, the ratios of the X-like dimer were not so different between the WT and K14E mutants, and the values were small in these cases (Fig. 2*A*).

We speculate that the existence of the SS-dimer interface affected the appearance of the X-like dimers because Lys14 facilitates SS-dimer formation, as previously reported (10–12). The presence of two populations of conformations, the X-dimer that facilitates SS-dimer formation and the X-dimer–like that does not, might have prevented a fair comparison of the ratios of the X-like dimers in WT and K14E mutants because the HS-AFM could not distinguish between the two conformations. The notable decrease in the ratio of the cross-shaped dimers (2%) in the SS-dimer–incompetent W2A–K14E mutant from that of the W2A (20%) supports this interpretation. Furthermore, the ratio of dimers observed by HS-AFM in nanomolar concentrations to distinguish individual dimers does not simply represent the ratio in near physiological conditions since the binding state of cadherins is affected by the concentration (44). The importance of the X-dimer–like conformations without Lys14 interactions should be further investigated in future studies.

Additionally, a comparative analysis of the HS-AFM images of the SS- and X-like dimers with their pseudo-AFM images of SS- and X-dimers simulated by the structural model based on the crystal structure showed that their overall structures were similar, whereas slight differences were observed in the X-like and X-dimers (Fig. 2*B–E* and *SI Appendix*, Fig. S7*F–H*). The comparison also revealed that the X-like dimers adsorbed flatly on the mica substrates with the convex sides of the protomers, indicating that the protomers were deformed while maintaining the dimeric form. The flexibility of ectodomains was supported by the results obtained for monomeric ectodomains twisting on the substrate (*SI Appendix*, Fig. S2*B and C*). The slight

differences between the actual HS-AFM images of the X-like dimers and pseudo-AFM images of the X-dimer may have also been caused by the intermittent mechanical contacting of the AFM probe perpendicularly to the binding interface of the X-like dimers during scanning. The orientation of the binding interface of the X-like dimers seemed to be more sensitive to the perpendicular force compared to that of the rigid SS- (W-shaped) dimers flattened on the substrate based on the possible orientations assumed by the structural modeling (*SI Appendix*, Fig. S7). X-dimers or X-dimer–like conformations in solution in a three-dimensional space should be further investigated in future studies.

Dynamic Features of S-Shaped Dimers. The HS-AFM images of the SS- and X-dimer mutants and WT showed that at least half of the population of dimers existed as S-shaped dimers (Fig. 2*A*). The simulated pseudo-AFM images for all orientations of the SS- and X-dimers did not show S-shaped or reverse S-shaped conformations (*SI Appendix*, Fig. S7*A* and *D*). We also confirmed that the inhibition of *cis*-binding interfaces between Val81 of EC1 and Leu175 of EC2 of the adjacent protomers did not affect the appearance of the S-shaped dimer (Fig. 2*A*) (17, 25). These results indicate that the S-shaped dimer forms by binding interfaces different from those of the SS- and X-dimers and *cis*-binding. Furthermore, we observed that the WT tagged with GFP on the membrane-proximal side had an S-shaped dimer formed at the membrane-distal sides of the ectodomains (Fig. 3). The HS-AFM images of the S-shaped dimer showed that the angle between the major axes along the protomer varied extensively, thereby changing the binding interfaces (Fig. 1*C* and *D*). The binding was not affected by fluctuations in the calcium binding sites of the ectodomains because of low Ca^{2+} concentrations (Fig. 5*C*). These results indicate that the membrane-distal tip regions of the ectodomains of E-cadherin dynamically interact and the interfaces are not highly dependent on a single residue, such as Trp2 and Lys14, for the SS- and X-dimers (10, 23, 45). The dynamic interactions between the S-shaped dimers also suggest that their binding is weaker than that of the X-like and SS-dimers.

In the present study, we could not determine the binding interfaces of the S-shaped dimers as it was difficult to identify the key residues, and thus, further mutational analyses could not be performed. Previous studies using X-ray crystallography have reported the dimeric structure of EC1 of N-cadherin and the interaction between EC1 and EC2 of P-cadherin formed by different binding interfaces from the SS- and X-dimers and *cis*-binding; however, the binding interfaces of these dimers were not identical (20, 29). These previous studies and the HS-AFM observations of the dynamic S-shaped dimers formed by the membrane-distal portions of the ectodomains with variable conformations in this study suggest the existence of weak interactions that are different from those of the SS- and X-dimers, and *cis*-binding.

Strand-Swap Dimerization and Dissociation Processes. The HS-AFM images of strand-swap dimerization and dissociation of the D1A mutant provided insights into the processes of strand-swap dimerization (Fig. 4). The quantitative analysis of the HS-AFM images revealed that the strand-swap dimerization and dissociation processes were completed within 0.9 s and the X-like dimers had both static and dynamic states, supporting previous NMR, force spectroscopy, and simulation studies (11, 12, 22). Based on the strand-swap dimerization and dissociation processes observed by the HS-AFM, we created a model of the transition processes among different dimeric conformations (Fig. 6). In this model, the dimerization and dissociation of SS-dimers could occur by flipping motion of the protomers from X- and S-shaped dimers. Previously, MD simulations of the EC1–EC2 of E-cadherin predicted the formation of the SS-dimer from the X-dimer by flipping motions (12). The X-dimer is considered to be an intermediate that brings EC1 close to its partner EC1 and decreases the kinetic barrier for strand-swap dimerization because the free energy (ΔG) of the strand-swapping process of the SS-dimer is similar to that of the insertion process of Trp2 into its own acceptor pocket in monomers (11, 13, 21).

In contrast, the X-dimer–incompetent K14E mutant also formed SS-dimers, although the formation reached equilibrium
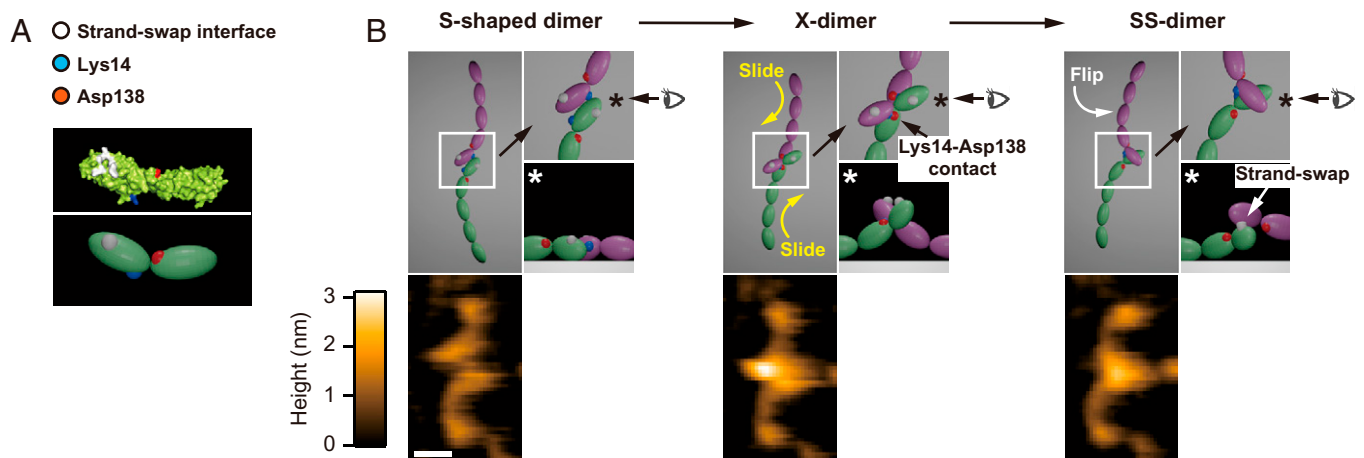
Fig. 6. Hypothesis of the strand-swap dimerization processes of E-cadherin based on HS-AFM observations. (*A*) Key residues in crystal structure and a simplified model. The upper image shows crystal structure of EC1–EC2 of E-cadherin (PDB ID code: 1Q1P). A part of core residues for strand-swap interface (Trp2, Lys25, Glu89, Asp90, and Met92) is colored in white. Lys14 and Asp138, which form a salt bridge in X-dimer interface, are colored in blue and red. The lower image shows a simplified model based on the upper image. White, blue, and red spheres in the bottom image indicate corresponding site of strand-swap interface, Lys14 and Asp138 shown by same colors in the upper image. Sizes of the spheres do not represent surface areas of the residues in the upper image. This model was used in *B*. (*B*) A hypothesis of the strand-swap dimerization processes modeled based on the HS-AFM observation in Fig. 4*A*. First, the X- (cross-shaped) dimer formed from the S-shaped dimer by sliding motions of protomers, indicated by yellow curved arrows. The SS- (W-shaped) dimer then formed from the X-dimer (or S-shaped dimer) by a flipping motion of one protomer, indicated by a white curved arrow. Lower HS-AFM images shows identical conformations in the upper models. (Scale bar, 10 nm.)

slowly (10, 11). The HS-AFM observation of the SS-dimer formation from S-shaped conformation suggests that the S-shaped dimer could also be an intermediate of SS-dimer formation, although the majority of SS-dimers are formed via X-dimers (11). We also hypothesized that X-dimer formation could occur through sliding motions of the S-shaped dimers in the initial binding processes (Fig. 6B). Although it has been shown that the X-dimer acts as an intermediate for SS-dimer formation, the role of the X-dimer in the initial cell–cell contact is counterintuitive, as the binding interfaces are located on the membrane-proximal side of the ectodomains (between EC1 and EC2) instead of the membrane-distal tip side (EC1). Structural variabilities and membrane-distal tip interactions of the S-shaped dimers and the SS-dimer formations from the S-shaped conformations observed by HS-AFM suggest that the S-shaped dimers contribute to X- and SS-dimer formation in the initial binding processes.

We also found that the X-like dimers of the W2A mutant changed the binding interface to the proximal side of the membrane, which was almost in the middle regions of the ectodomains, although we could not identify the relationship with the strand-swap dimerization discussed above (*SI Appendix*, Fig. S14 and Movie S9). Previous studies using force spectroscopies and bead aggregation assays have shown the contribution of EC1 and EC2 as well as other EC domains in cadherin binding, supporting the dimeric structure formed by the near middle regions of the ectodomains observed using HS-AFM in this study (28, 30, 31). Several studies have reported that type I cadherins form multiple binding complexes, supporting the multiple dimeric structures observed using HS-AFM (20, 28–31). The multiple binding properties of cadherins are influenced by scaffolds, which affect the binding probabilities, and these features are especially important for forming clusters of ectodomains (8, 25–27). The SS-dimer is thought to be the main component of the cadherin cluster (17, 25), whereas the contribution of other dimeric structures to clustering remains unclear. In this study, we directly visualized the transitions among different dimeric structures; however, the dimers did not form clusters. Reconstitution experiments using liposomes successfully induced the formation of artificial cadherin clusters (25, 46). This type of lipid-based reconstitution of other membrane proteins has been applied in studies involving HS-AFM (47, 48). Directly visualizing cadherin clusters using HS-AFM and the reconstitution method may be a solution for further investigation of the process of cadherin clustering in future studies.

In summary, the direct visualization of E-cadherin in solution using HS-AFM revealed multiple dimeric structures, which were mainly classified into SS- (W-shaped), X-like (cross-shaped), and S-shaped dimers. Mutational analyses, structural modeling, and the structural dynamics of SS-dimer formation suggest that the dynamic interactions of the S-shaped dimers, which are formed in membrane-distal ectodomains, contribute to the formation of X- and SS-dimers. The direct visualization of multiple dimeric structures and dimerization processes of E-cadherin in solution at a single-molecule resolution provides insights into the contribution of dynamic interactions to X- and SS-dimer formation in type I cadherins.

Materials and Methods

DNA Construction. To express mouse E-cadherin ectodomains in HEK293T cells, the expression plasmid pcDNA3.1/V5-His A (Cat# V810-20; Thermo Fisher Scientific) was used. A DNA fragment encoding the N-terminal 700-amino acid region of mouse E-cadherin (amino acids 1 to 700; UniProtKB/Swiss-Prot:

P09803.1) (2) containing the prodomain region was amplified by PCR using a forward primer (5′-GCCATGGGAGCCCGGTGCCGCAG-3′) and reverse primer (5′-AGCAGCAGCAGCCGCCTTCATGCAGTTGTTGACC-3′). The E-cadherin–encoding plasmid used for amplification was a gift from Hiroki Oda, JT Biohistory Research Hall, Takatsuki, Japan. The amino acid position was numbered starting from Asp157 as the first N-terminal amino acid of mature ectodomains (Asp1-Ala544) in this study. A DNA fragment encoding EGFP was amplified by PCR using forward (5′-GCGGCTGCTGCTGCTGCTAGCAAGGGCGAGGAG-3′) and reverse (5′-CTTGTACAGCTCGTCCATGCCG-3′) primers. The EGFP-encoding plasmid used for amplification was pAcHis-DEEC6-EGFP-His (49). A DNA fragment encoding pcDNA3.1/V5-His A was amplified by PCR using a forward primer (5′-GACGAGCTGTACAAGTCTAGAGGGCCCCTTCGAAGG-3′) and reverse primer (5′-CCGGGCTCCCATGGCGAATTCCACCACACTGGAC-3′). The DNA fragments of E-cadherin, EGFP, and pcDNA3.1/V5-His A were fused using the In-Fusion HD Cloning Kit (Cat# 639633; Takara Bio) and designated as pcDNA-MEEC1-5-EGFP-V5-His (WT-GFP), which contained V5 and His tag sequences on the C-terminal side. The pcDNA-MEEC1-5-EGFP-V5-His was used as a template for other constructs, as listed in *SI Appendix*, Table S1. Two fragments from the amplification of each construct, listed in *SI Appendix*, Table S1, were fused using the In-Fusion HD Cloning Kit. All constructs had a V5-His tag sequence on the C-terminal side.

Cell Culture and Protein Purification. HEK293T cells were cultured at 37 °C in 5% CO_2 in DMEM (Cat# 10569010; Thermo Fisher Scientific) supplemented with 10% heat-inactivated fetal bovine serum (Cat# 10569010; MP Biomedical). All transfections were performed using the TransIT-LT1 Transfection Reagent (Cat# MIR2300; Mirus Bio) according to the manufacturer's instructions. HEK293T cells were seeded at a density of 3×10^5/mL in 10 mL of medium in a 100-mm dish (Cat# TR4002; Nippon Genetics) ~16 h before transfection. Fifteen micrograms of plasmid DNA were used for each transfection. After 3 d of incubation, the conditioned medium containing secreted V5-His-tagged proteins was collected and centrifuged at $2,600 \times g$ for 5 min at 25 °C to obtain 9 mL of supernatant, which was passed through a 0.22-μm pore-size filter (Cat# SLGPR33RS; Merck KGaA). To cleave off the prodomains of the ectodomains of E-cadherin, the supernatants were treated with trypsin (124 unit/mL; Cat# 18172–94; Nacalai Tesque) for 10 min at 25 °C. The reaction was immediately quenched with trypsin inhibitor (600 unit/mL; Cat# 202-09221; Fujifilm Wako Pure Chemical). To purify V5-His-tagged proteins from the supernatants, a V5-tagged protein magnetic purification kit (Cat# 3341; Medical & Biological Laboratories) was used according to the manufacturer's instructions. The purified proteins were stored in PBS containing 1 mM $CaCl_2$ at 4 °C until further use. The purified proteins were separated on a 12.5% polyacrylamide gel (Cat# 199-14971; Fujifilm Wako Pure Chemical), analyzed by Coomassie brilliant blue staining, and a fragment of ~80 kDa was confirmed as the matured ectodomains of E-cadherin (*SI Appendix*, Fig. S1A) (50). HS-AFM was performed for up to 1 wk after purification.

Bead Aggregation Assay. Five microliters of anti-His–tagged magnetic beads (Cat# D291-11; Medical & Biological Laboratories) and 5 μL of purified V5-His-tagged protein solution were mixed in a 1.5-mL tube and incubated for 15 min at 25 °C. The bead suspensions were diluted in 1 mL of HC (20 mM Hepes and 4 mM $CaCl_2$ adjusted with NaOH to pH 6.8) or HE (20 mM Hepes (pH 6.8) and 10 mM EGTA) buffer and transferred to a 12-well suspension culture plate (Cat# 665102; Greiner Bio-One). This was followed by a 1-h rotation at 180 rpm on a horizontal shaker (MMS-3010; Tokyo Rikakikai) at 25 °C. The plate was then slowly moved to the stage of an inverted microscope (IX73; Olympus). Images of bead distribution were captured to obtain a single image (1,920 × 1,200 pixels) for each well using a 10× objective lens and digital color camera (DP74; Olympus). Images were trimmed to 1,200 × 1,200 pixels using ImageJ 1.51d software (NIH) (51). We confirmed previous observations where the purified ectodomains of WT induced bead or cell aggregation and SS- or X-dimer–incompetent mutations (W2A and K14E) abolished or decreased aggregation (*SI Appendix*, Fig. S1B) (10, 13).

Protein Preparation for HS-AFM. A mica substrate with a diameter of 1.5 mm and thickness of 0.1 mm (Furuuchi Chemical) was attached with glue on a glass stage. A 2-μL droplet of 0.04% 3-aminopropyltriethoxysilane (APTES) solution was placed on a freshly cleaved mica substrate and incubated for 3 min. The APTES-mica substrate was then washed twice with 80 μL of Milli-Q water. A 2-μL droplet

of purified protein solution was placed on the APTES-mica substrate for 5 min and washed with 80 µL of HC buffer. The concentration of purified proteins for adsorption was adjusted based on the pilot observations.

HS-AFM. HS-AFM was performed in HC buffer at room temperature (25 °C) using a laboratory-built HS-AFM instrument operated in tapping mode (32). BL-AC10DS-A2 cantilevers (Olympus) with a length of 9 µm, width of 2 µm, thickness of 0.13 µm, spring constant of ~0.1 Nm⁻¹, and resonant frequencies of 400 to 500 kHz were used. The carbon tip at the end of the cantilever was grown by electron beam deposition and sharpened by argon gas etching to a tip radius of 2 to 5 nm (52). The free oscillation amplitude of the cantilever was set to 1 to 2 nm, and the setpoint of the amplitude for feedback control was ~80% of the free amplitude during scanning. HS-AFM in low calcium concentrations or without calcium was performed in 20 mM Hepes (pH 6.8) with 0.01 mM $CaCl_2$ or 10 mM EGTA. For the HS-AFM of the conformational transition of cadherin due to the removal of Ca^{2+}, purified proteins were adsorbed on 0.01% APTES-mica substrate in 20 mM Hepes (pH 6.8) with 1 mM $CaCl_2$, and then EGTA solution was added at a final concentration of 3 mM using a pipette. Two or more independent protein purifications and HS-AFM were performed for each recombinant protein. All AFM images obtained in this study were deposited in the Mendeley Data Repository (53).

HS-AFM Image Processing and Analysis. HS-AFM image processing was performed using the laboratory-made analysis software FalconViewer based on Igor Pro-8 (WaveMetrics). The angle between the major axes of the protomers of cadherin dimers (Fig. 1*C* and *SI Appendix*, Fig. S3) was measured using ImageJ 1.51d software (NIH) (51). The angle distributions from sequential images of the dimers (*SI Appendix*, Fig. S3) were measured using up to 20 frames of HS-AFM images in each dimer of the 71 WT dimers. Fitting two Gaussians to the data of angles (φ) of dynamic dimers presented in *SI Appendix*, Fig. S3*C* had a smaller fitting error (χ^2) than in the case of fitting a single Gaussian, and the distributions were well separated using these two peaks (53). However, when fitting three Gaussians to the data, the third peak distribution fully overlapped the major distribution. Therefore, we selected the two Gaussians, leading to the majority and minority. The numerical data obtained in this study were deposited in the Mendeley Data Repository (53).

Structural Modeling. SS- and X-dimer structures consisting of full-length ectodomains (EC1 to EC5) of E-cadherin were modeled using BIOVIA Discovery Studio 2017 R2 (Dassault Systèmes) by fitting the EC1–EC2 parts of the full-length ectodomains (PDB ID code: 3Q2V chain A) (25) to both sides of the SS- and X-dimers formed by EC1–EC2 (PDB ID codes: 2QVF and 3LNH) (10), respectively. Based on these full-length ectodomain structures, pseudo-AFM images of the SS- and X-dimers (Fig. 2*B* and *D* and *SI Appendix*, Fig. S7*A* and *D*) were produced using the laboratory-made analysis software FalconViewer based on Igor Pro-8 (WaveMetrics) by setting the paraboloid-shaped tip of the AFM probe with a tip radius of 0.5 nm. The images were processed using a low-pass filter with a cutoff frequency of 2 nm. A modified model structure of the X-dimer (shown in *SI Appendix*, Fig. S7*E*) was created to orient the EC3–EC5 region more flatly on the substrate, by rotating the dihedral angle φ of Lys212 (in the EC2–EC3 linker) to 180°. Models of the ectodomains and dimers (Fig. 6) were produced using Blender 2.93.5 (Blender Foundation). The pseudo-AFM images obtained in this study were deposited in the Mendeley Data Repository (53).

Data Availability. All AFM image files and numerical data have been deposited in Mendeley Data Repository, https://data.mendeley.com/datasets/6xjzvcj774/3 (53).

Author affiliations: ᵃDepartment of Creative Research, Exploratory Research Center on Life and Living Systems, National Institutes of Natural Sciences, 444-8787 Okazaki, Japan; ᵇSchool of Life Science and Technology, Tokyo Institute of Technology, 226-8501 Yokohama, Japan; ᶜDepartment of Physics, Nagoya University, 464-8602 Nagoya, Japan; and ᵈInstitute for Glyco-core Research, Nagoya University, 464-8602 Nagoya, Japan

1. A. W. Koch, S. Pokutta, A. Lustig, J. Engel, Calcium binding and homoassociation of E-cadherin domains. *Biochemistry* **36**, 7697–7705 (1997).
2. A. Nagafuchi, Y. Shirayoshi, K. Okazaki, K. Yasuda, M. Takeichi, Transformation of cell adhesion properties by exogenously introduced E-cadherin cDNA. *Nature* **329**, 341–343 (1987).
3. M. Takeichi, Dynamic contacts: Rearranging adherens junctions to drive epithelial remodelling. *Nat. Rev. Mol. Cell Biol.* **15**, 397–410 (2014).
4. G. Berx, F. van Roy, Involvement of members of the cadherin superfamily in cancer. *Cold Spring Harb. Perspect. Biol.* **1**, a003129 (2009).
5. T. J. C. Harris, U. Tepass, Adherens junctions: From molecules to morphogenesis. *Nat. Rev. Mol. Cell Biol.* **11**, 502–514 (2010).
6. T. Lecuit, A. S. Yap, E-cadherin junctions as active mechanical integrators in tissue dynamics. *Nat. Cell Biol.* **17**, 533–539 (2015).
7. J. Brasch, O. J. Harrison, B. Honig, L. Shapiro, Thinking outside the cell: How cadherins drive adhesion. *Trends Cell Biol.* **22**, 299–310 (2012).
8. D. Leckband, S. Sivasankar, "Biophysics of cadherin adhesion" in *Adherens Junctions: From Molecular Mechanisms to Tissue Development and Disease*, T. J. C. Harris, Ed. (Springer, 2012), pp. 63–88.
9. L. Shapiro, W. I. Weis, Structure and biochemistry of cadherins and catenins. *Cold Spring Harb. Perspect. Biol.* **1**, a003053 (2009).
10. O. J. Harrison *et al.*, Two-step adhesive binding by classical cadherins. *Nat. Struct. Mol. Biol.* **17**, 348–357 (2010).
11. Y. Li *et al.*, Mechanism of E-cadherin dimerization probed by NMR relaxation dispersion. *Proc. Natl. Acad. Sci. U.S.A.* **110**, 16462–16467 (2013).
12. K. Manibog *et al.*, Molecular determinants of cadherin ideal bond formation: Conformation-dependent unbinding on a multidimensional landscape. *Proc. Natl. Acad. Sci. U.S.A.* **113**, E5711–E5720 (2016).
13. S. Sivasankar, Y. Zhang, W. J. Nelson, S. Chu, Characterizing the initial encounter complex in cadherin adhesion. *Structure* **17**, 1075–1081 (2009).
14. J. Vendome *et al.*, Structural and energetic determinants of adhesive binding specificity in type I cadherins. *Proc. Natl. Acad. Sci. U.S.A.* **111**, E4175–E4184 (2014).
15. B. Nagar, M. Overduin, M. Ikura, J. M. Rini, Structural basis of calcium-induced E-cadherin rigidification and dimerization. *Nature* **380**, 360–364 (1996).
16. O. Pertz *et al.*, A new crystal structure, Ca^{2+} dependence and mutational analysis reveal molecular details of E-cadherin homoassociation. *EMBO J.* **18**, 1738–1747 (1999).
17. T. J. Boggon *et al.*, C-cadherin ectodomain structure and implications for cell adhesion mechanisms. *Science* **296**, 1308–1313 (2002).
18. D. Häussinger *et al.*, Proteolytic E-cadherin activation followed by solution NMR and X-ray crystallography. *EMBO J.* **23**, 1699–1708 (2004).
19. E. Parisini, J. M. G. Higgins, J. H. Liu, M. B. Brenner, J. H. Wang, The crystal structure of human E-cadherin domains 1 and 2, and comparison with other cadherins in the context of adhesion mechanism. *J. Mol. Biol.* **373**, 401–411 (2007).
20. L. Shapiro *et al.*, Structural basis of cell-cell adhesion by cadherins. *Nature* **374**, 327–337 (1995).
21. S. Kudo, J. M. M. Caaveiro, K. Tsumoto, Adhesive dimerization of human P-cadherin catalyzed by a chaperone-like mechanism. *Structure* **24**, 1523–1536 (2016).
22. R. Koirala *et al.*, Inside-out regulation of E-cadherin conformation and adhesion. *Proc. Natl. Acad. Sci. U.S.A.* **118**, e2104090118 (2021).
23. K. Manibog, H. Li, S. Rakshit, S. Sivasankar, Resolving the molecular mechanism of cadherin catch bond formation. *Nat. Commun.* **5**, 3941 (2014).
24. S. Rakshit, Y. Zhang, K. Manibog, O. Shafraz, S. Sivasankar, Ideal, catch, and slip bonds in cadherin adhesion. *Proc. Natl. Acad. Sci. U.S.A.* **109**, 18815–18820 (2012).
25. O. J. Harrison *et al.*, The extracellular architecture of adherens junctions revealed by crystal structures of type I cadherins. *Structure* **19**, 244–256 (2011).
26. C. J. Thompson, V. H. Vu, D. E. Leckband, D. K. Schwartz, Cadherin extracellular domain clustering in the absence of trans-interactions. *J. Phys. Chem. Lett.* **10**, 4528–4534 (2019).
27. Y. Wu, J. Vendome, L. Shapiro, A. Ben-Shaul, B. Honig, Transforming binding affinities from three dimensions to two with application to cadherin clustering. *Nature* **475**, 510–513 (2011).
28. S. Chappuis-Flament, E. Wong, L. D. Hicks, C. M. Kay, B. M. Gumbiner, Multiple cadherin extracellular repeats mediate homophilic binding and adhesion. *J. Cell Biol.* **154**, 231–243 (2001).
29. A. Dalle Vedove, A. P. Lucarelli, V. Nardone, A. Matino, E. Parisini, The X-ray structure of human P-cadherin EC1-EC2 in a closed conformation provides insight into the type I cadherin dimerization pathway. *Acta Crystallogr. F Struct. Biol. Commun.* **71**, 371–380 (2015).
30. Q. Shi, V. Maruthamuthu, F. Li, D. Leckband, Allosteric cross talk between cadherin extracellular domains. *Biophys. J.* **99**, 95–104 (2010).
31. S. Sivasankar, W. Brieher, N. Lavrik, B. Gumbiner, D. Leckband, Direct molecular force measurements of multiple adhesive interactions between cadherin ectodomains. *Proc. Natl. Acad. Sci. U.S.A.* **96**, 11820–11824 (1999).
32. T. Ando *et al.*, A high-speed atomic force microscope for studying biological macromolecules. *Proc. Natl. Acad. Sci. U.S.A.* **98**, 12468–12472 (2001).
33. T. Uchihashi, C. Ganser, Recent advances in bioimaging with high-speed atomic force microscopy. *Biophys. Rev.* **12**, 363–369 (2020).
34. C. Ciatto *et al.*, T-cadherin structures reveal a novel adhesive binding mechanism. *Nat. Struct. Mol. Biol.* **17**, 339–347 (2010).
35. P. Katsamba *et al.*, Linking molecular affinity and cellular specificity in cadherin-mediated adhesion. *Proc. Natl. Acad. Sci. U.S.A.* **106**, 11594–11599 (2009).
36. J. Vendome *et al.*, Molecular design principles underlying β-strand swapping in the adhesive dimerization of cadherins. *Nat. Struct. Mol. Biol.* **18**, 693–700 (2011).

37. A. Royant, M. Noirclerc-Savoye, Stabilizing role of glutamic acid 222 in the structure of enhanced green fluorescent protein. *J. Struct. Biol.* **174**, 385–390 (2011).

38. S. Hong, R. B. Troyanovsky, S. M. Troyanovsky, Cadherin exits the junction by switching its adhesive bond. *J. Cell Biol.* **192**, 1073–1083 (2011).

39. O. Y. Laur, J. Klingelhöfer, R. B. Troyanovsky, S. M. Troyanovsky, Both the dimerization and immunochemical properties of E-cadherin EC1 domain depend on Trp([156]) residue. *Arch. Biochem. Biophys.* **400**, 141–147 (2002).

40. R. B. Troyanovsky, O. Laur, S. M. Troyanovsky, Stable and unstable cadherin dimers: Mechanisms of formation and roles in cell adhesion. *Mol. Biol. Cell* **18**, 4343–4352 (2007).

41. W. He, P. Cowin, D. L. Stokes, Untangling desmosomal knots with electron tomography. *Science* **302**, 109–113 (2003).

42. M. Sikora et al., Desmosome architecture derived from molecular dynamics simulations and cryo-electron tomography. *Proc. Natl. Acad. Sci. U.S.A.* **117**, 27132–27140 (2020).

43. T. Shibata-Seki, M. Nagaoka, M. Goto, E. Kobatake, T. Akaike, Direct visualization of the extracellular binding structure of E-cadherins in liquid. *Sci. Rep.* **10**, 17044 (2020).

44. V. Z. Miloushev et al., Dynamic properties of a type II cadherin adhesive domain: Implications for the mechanism of strand-swapping of classical cadherins. *Structure* **16**, 1195–1205 (2008).

45. M. Sotomayor, K. Schulten, The allosteric role of the Ca^{2+} switch in adhesion and elasticity of C-cadherin. *Biophys. J.* **94**, 4621–4633 (2008).

46. O. Lambert et al., The basic framework of VE-cadherin junctions revealed by cryo-EM. *J. Mol. Biol.* **346**, 1193–1196 (2005).

47. Y.-C. Lin, C. Chipot, S. Scheuring, Annexin-V stabilizes membrane defects by inducing lipid phase transition. *Nat. Commun.* **11**, 230 (2020).

48. M. Shibata et al., Oligomeric states of microbial rhodopsins determined by high-speed atomic force microscopy and circular dichroic spectroscopy. *Sci. Rep.* **8**, 8262 (2018).

49. S. Nishiguchi, A. Yagi, N. Sakai, H. Oda, Divergence of structural strategies for homophilic E-cadherin binding among bilaterians. *J. Cell Sci.* **129**, 3309–3319 (2016).

50. M. Ozawa, R. Kemler, Correct proteolytic cleavage is required for the cell adhesive function of uvomorulin. *J. Cell Biol.* **111**, 1645–1650 (1990).

51. J. Schindelin et al., Fiji: An open-source platform for biological-image analysis. *Nat. Methods* **9**, 676–682 (2012).

52. M. Wendel, H. Lorenz, J. P. Kotthaus, Sharpened electron beam deposited tips for high resolution atomic force microscope lithography and imaging. *Appl. Phys. Lett.* **67**, 3732–3734 (1995).

53. S. Nishiguchi, T. Furuta, T. Uchihashi, Multiple dimeric structures and strand-swap dimerization of E-cadherin in solution visualized by high-speed atomic force microscopy. Mendeley Data. https://data.mendeley.com/datasets/6xjzvcj774/3. Deposited 11 June 2022.